Hindawi
International Journal of Aerospace Engineering
Volume 2022, Article ID 6847331, 9 pages
https://doi.org/10.1155/2022/6847331

Research Article

Performance Improvement for Single-Photon LiDAR with Dead Time Selection

Lei Feng,[1] **Fenglin Wang**,[1] **Meng An**,[2] **and Qiang Zhang**[2]

[1]*Beijing Institute of Tracking and Telecommunication Technology, Beijing 100094, China*
[2]*Institute of Spacecraft System Engineering CAST, Beijing 100094, China*

Correspondence should be addressed to Lei Feng; fenglei_798@163.com

Received 1 April 2022; Revised 7 May 2022; Accepted 31 May 2022; Published 1 July 2022

Academic Editor: Keke Shi

Compared with the impulse LiDAR, the single-photon LiDAR has higher measurement sensitivity in the prominent feature, especially for space-based long-distance imaging. The distance measurement and the detection probability are the critical performance for LiDAR. The ranging of single-photon LiDAR is mainly different from the photon ranging of pulsed LiDAR. Dead time has a significant effect on distance measurement accuracy and detection probability, which are key parameters for detectors when implementing sound control. Therefore, the model of detector dead time, measurement accuracy, and detection probability should be established, and simulation results that meet application requirements should be achieved. Based on the single-photon ranging theory, the dead time, measurement accuracy, and detection probability model of single-photon LiDAR are studied. Furthermore, the systematic simulation of different contrasts is carried out according to the model. The simulation results demonstrate that the model can accurately perform the relationship between dead time and single-photon LiDAR system parameters. The research results can prove the design and verification of single-photon LiDAR dead time.

1. Introduction

The traditional space-based LiDAR ranging uses a linear pulse detection system with low detection sensitivity. It relies on a high threshold-to-noise ratio to distinguish the echo signal from the background noise. Hence, the required laser energy aperture product is significantly large. The laser echo pulse contains at least thousands of photons of energy [1]. On the one hand, the high laser emission energy limits the repetition frequency of the emitted laser, the data sampling rate, and the detection distance. On the other hand, a large number of echo photons are wasted. The advantage of photon-counting laser ranging technology is that it can obtain distance information of long-distance targets with lower laser pulse energy, thereby increasing the number of beams, reducing the system's requirements for space-based satellite platforms such as power consumption and telescope aperture, and improving system performance, time resolution accuracy, and detection accuracy. The single-photon multimode LiDAR detector adopts a new single-photon system with the detector output energy according to photons [2]. The single-photon detection efficiency and dark count are determined by the dead time of the system. Thus, the dead time of the single-photon detector directly affects the detection of the system. Efficiency and dark count size will ultimately affect the bit error rate, affecting system indicators such as LiDAR detection probability and ranging accuracy.

It is worth noting that the single-photon LiDAR can be used for relative position and velocity control in spacecraft rendezvous and docking with high precision, which can also be adopted in distributed space systems, e.g., satellite constellation, satellite swarm, and federated satellite, including many satellites distributed in different orbits cooperating with each other to perform a very complex space mission [3–5]. However, the measurement of single-photon LiDAR may cause measurement errors or input delay. After docking, for combined spacecraft attitude control problem with the unknown measurement delay and input delay, the work in [6] investigated a novel intermediate-observer to achieve effective stabilization. Nevertheless, the time-delay was only considered, such that the application of this approach was relatively conservative. Much literature has made great

contributions to spacecraft control, most of which depends on that the state information can be known exactly and applied to control instructions directly. In fact, the single-photon LiDAR can make sense to provide the state information [7–9].

In this paper, according to the working principle of single-photon detection, the relationship model between the dead time of the single-photon detector, ranging accuracy, and detection probability is established, and the correctness of the relationship model is verified by simulation under different contrasts. Finally, combined with the free-form surface spectroscopy system, simulations verify the relationship between dead time and probe illumination. The simulation results show that the relational model proposed in this paper can be applied to the determination of the dead time of the single-photon LiDAR detector and the design and verification of the index control.

2. Principle Analysis of Single-Photon Laser Detection

The schematic diagram of the working principle for single-photon laser detection is shown in Figure 1.

Single-photon LiDAR is a photon-counting system. The system completes laser ranging through photon counting [10]. Based on pulsed laser ranging, the introduction of time correlation conforms to single-photon counting, and the linear detection system contains many photons. The detection of the echo waveform is converted into a count for a single echo photon event, making full use of the single-photon level energy in the echo signal, using the correlation of the target distance information and the cumulative count of photon events in the background noise and dark counts. The actual distance data is extracted to improve the detection probability and maximize the system's detection sensitivity and efficiency. The histogram statistics of photon event detection of echo signal based on time correlation are shown in Figure 2. In this figure, the abscissa is the number of single-photon events and the number of transmitted pulses, and the ordinate is the ranging elevation accuracy.

Unlike the imaging method of CCD or CIS image sensor that is usually used in traditional LiDAR to read the sound charge, single-photon LiDAR generally uses a single-photon avalanche diode [11]. After the array is integrated, the ranging function is realized.

A single-photon avalanche diode is an avalanche photodiode that operates in the Geiger mode [12, 13]. A continuous avalanche breakdown occurs when photons strike the active region of the diode, so a quench circuit is required to stop the avalanche process. Therefore, the output voltage from the avalanche to the end of quenching appears as a single pulse signal one after the other, and one pulse corresponds to one photon. The periodic pulse signal can be output as a pulse square wave signal one by one after the shaping circuit, and the counter can record the number. The light intensity can be quantified by counting the number of pulses, and a detector array composed of multiple single-photon avalanche diodes can be used as a detection device.

3. Dead Time Impact Analysis

Many factors affect the ranging accuracy of single-photon LiDAR, and the modeling process is complicated. The main factors related to single-photon detectors are the influence of the dead time of the avalanche diode on the effective receiving aperture modeling and the dead time of the detector on the ranging accuracy [14].

3.1. Detector Dead Time Effect on the Effective Receiver Aperture. For each laser pulse detection, the existence of any dead time will limit the number of signal photon events [15]. Suppose the receiver dead time τ_d is greater than the signal photon distribution time τ_s, less than the time corresponding to the distance sampling interval τ_b, and the number of signal photons reaches the upper limit. The contrast ratio is shown in the following formula:

$$\lim_{n_s \gg 1} C_d = 1 - \frac{\tau_d}{\tau_b} + \frac{1}{n_b}. \tag{1}$$

In the above formula, C_d is the contrast when the number of signal photons reaches the upper limit, n_s is the average number of signal photons, n_b is the average number of photons sampled for each distance, τ_d is the receiver dead time, and τ_b is the time corresponding to the distance sampling interval. When the dead time of the detector or receiver exceeds the distribution of echo signal photons, only one photon in the signal photon stream can be effectively detected, and any redundant signal photons cannot be detected [16]. Due to the existence of the received dead time, when the extreme situation occurs, that is, the signal photon appears within the dead time range of the detector, the signal photon will not be detected at this time, and the noise photon that triggers the detector will be the signal photon event by default. It brings a sizeable ranging error [17]. Since each pixel works independently and does not affect each other for multielement detectors, more signal photons can be obtained in a single laser pulse. The utilization rate of signal photons is significantly increased. At the same time, the background noise photons are distributed to more pixels. When designing the system, the aperture of the leading optical component of the receiver can be appropriately increased, which reduces the requirement for the single-pulse energy of the transmitter [18]. Using a multielement single-photon detector, the maximum allowable effective receiving area is shown in

$$\begin{aligned} A_r &= \frac{1}{\beta/N_P\left[\tau_b C_d - 1/1 - \exp\left(-n_s/N_p\right) + \tau_d\right]} \\ &\approx \frac{N_1}{\beta\tau_b\left[(C_d - 1) + (1 - e^{-n_p})\tau_d/\tau_b\right]}. \end{aligned} \tag{2}$$

In formula (2), A_r is the maximum allowable effective receiving area, C_d is the contrast when the number of signal photons reaches the upper limit, n_s is the average number of signal photons, τ_d is the receiver dead time, τ_s is the signal photon distribution time, and τ_b is the time corresponding

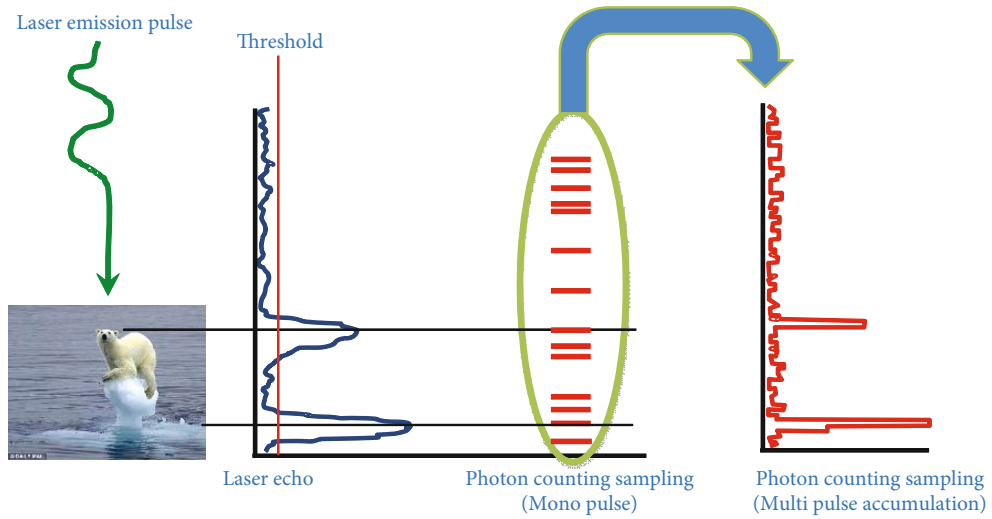

Figure 1: Operation schematic diagram for single-photon laser detection.

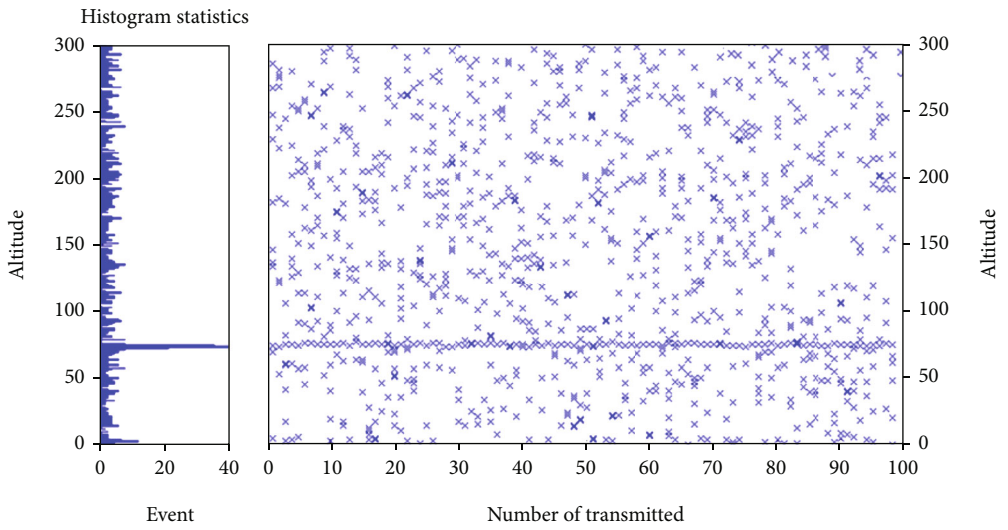

Figure 2: Statistical histogram for time-related back wave signal photon event detection.

to the distance sampling interval. β is the composite noise count rate per unit area of the receiver, N_p is the number of pixels received by the detector, and N_1 is the signal photon count event acquired by the detector. $N_1 \approx N_p(1 - e^{-n_p})$, within $n_p = n_s/N_p$, n_s is the number of signal photons incident on the photosensitive surface of the detector. The modeling and simulation of the unit detector and the 16-element detector are carried out. Assuming that the receiver dead time is 16 ns and the average signal photon number is 6, the relationship between the effective receiving aperture of the main optical component of the receiver and the signal contrast is shown in Figure 3.

Figure 3 is the dead time of the unit detector and the 16-element detector receiver, respectively. Under the condition of the average number of signal photons $n_s = 6$, when the system adopts unit detectors and multielement detectors, the simulation results of the relationship between the maximum allowable effective receiving aperture of the receiver and the signal contrast show that with the increase of the number of detector elements, under the same signal contrast, the required practical receiving the size of the caliber becomes more significant, and the same model relationship is satisfied.

At the same time, under the condition that the signal contrasts are $C = 2, 3, 5, 10$, respectively, this paper analyzes the relationship between the effective receiving aperture of the optical component and the receiving dead time of the detector as shown in Figure 4.

Figure 4 shows the relationship between the maximum allowable effective receiving aperture of the receiver and the signal contrast when the system uses a unit detector and a multielement detector under the condition that the signal contrasts are $C = 2, 3, 5, 10$, respectively. Through simulation analysis, to ensure the same signal contrast, multielement detectors can increase the allowable receiving area by about 4-6 times compared with single-pixel detectors.

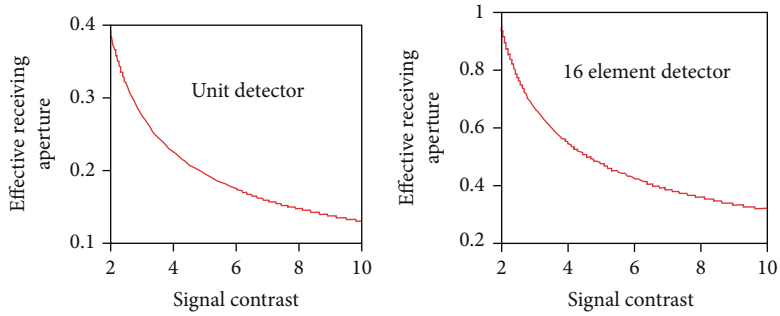

Figure 3: Contrast and effective aperture for single-pixel detector and 16 detectors.

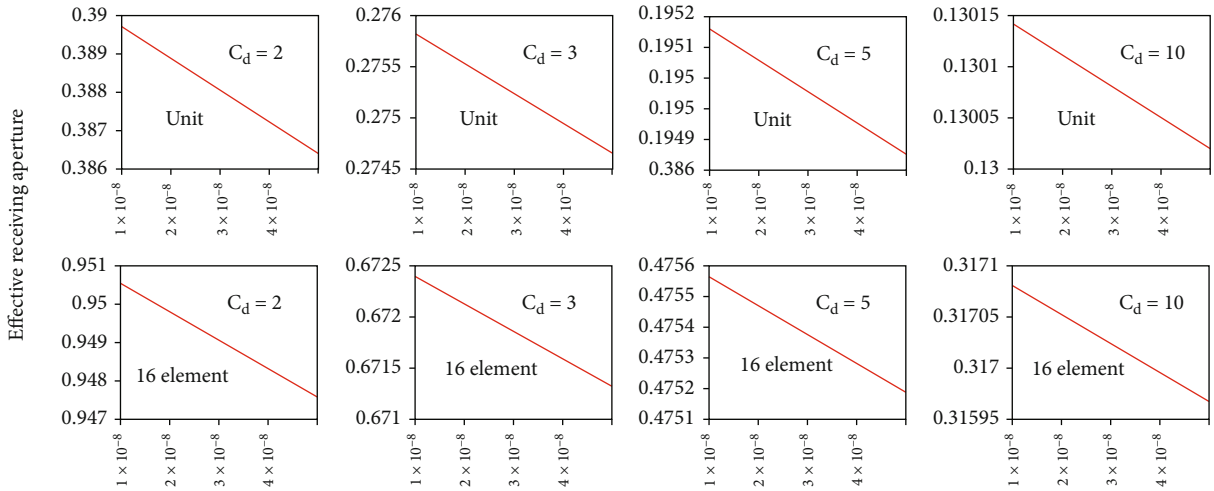

Figure 4: LiDAR receiver dead time and effective receive aperture relationship.

According to the above analysis, for example, the dead time of the detector is 16 ns, the number of pixels is 16, and the contrast is 3. According to the maximum aperture constraint, the aperture is 1000 mm.

3.2. The Detector Dead Time Influence on Ranging Accuracy. The dead time of the LiDAR receiver directly affects the ranging accuracy of the integrated load system. To reduce the impact of dead time on ranging accuracy, it is necessary to integrate the photosensitive surface of each single-photon detector into its detection circuit [19–21]. By receiving 4×4 pixels of a single laser footprint, the dead time of the detection link is reduced, the limitation of the dead time on the receiving aperture is also reduced, and the ranging accuracy is improved. Assuming that the number of multibeam ranging channels is 1000, the size of the detection array is 4000×4. The pixel assignment is shown in Figure 5.

In the working process of LiDAR, the echo pulse width is widened due to the influence of beam divergence angle, ground slope, and roughness. The widening effect is more pronounced if the measurement object is a cloud, tree canopy, and other penetrating targets or soft targets. The probability that the signal photon triggers the photon detector in the time range $f(\tau, \tau + d\tau)$ is equal to the product of the detection probability in the unit time range and the probability that it is not triggered in the previous unit time range, as shown in

$$P(\tau)d\tau = C_N s(\tau)d\tau \left\{ \int_{\tau-\tau_d}^{\tau} d\tau' s\left(\tau'\right) \right\}, \tag{3}$$

where $\tau = t - 2h_0/c$ is the difference between the pulse emission time and the optical path time reaching the center of the beam. h_0 is the optical path of the pulse to the center of the beam. $s(\tau)$ is the signal waveform arriving at the detector (or it can be more accurately defined as the Poisson generation function). C_N is the detection probability, and τ_d is the receiver dead time. The contribution of detector pixels to small noise counting events in the echo pulse time domain is not considered in (3). The contribution of background noise events to the whole photon-counting event is limited to one distance sampling interval. The system deviation and ranging accuracy for the unit detector are expressed as follows:

$$\begin{aligned} \langle \Delta R \rangle &= \frac{C}{2} \langle \tau \rangle, \\ \Delta R_{\mathrm{RMS}} &= \frac{C}{2} \sqrt{\langle \tau^2 \rangle - \langle \tau \rangle^2}, \end{aligned} \tag{4}$$

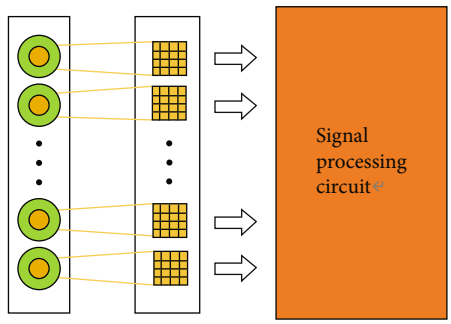

Figure 5: Size of the single-photon detector.

where $\langle \Delta R \rangle$ is the systematic deviation, ΔR_{RMS} is the root mean square of system ranging accuracy, and $\langle \tau \rangle$ and $\langle \tau^2 \rangle$ are the average value and mean square value of pulse broadening probability distribution in (3), respectively. Relative to pulse broadening, for extreme cases where the dead time is very small ($\tau_d \ll \tau_c$) or very large ($\tau_d \gg \tau_c$), the specific form is shown in

$$P_0(\tau)d\tau = \frac{1}{n_s} s(\tau)d\tau, \tag{5}$$

$$P_\infty(\tau)d\tau = \frac{1}{1-e^{-n_s}} d\tau \cdot s(\tau) \cdot \exp\left\{-\int_{-\infty}^{\tau} d\tau' s\left(\tau'\right)\right\}, \tag{6}$$

where $P_0(\tau)d\tau$ is the probability of triggering the photon detector within the time range of $(\tau, \tau + d\tau)$ when the dead time is very small ($\tau_d \ll \tau_c$), $P_\infty(\tau)d\tau$ is the probability of triggering the photon detector within the time range of $(\tau, \tau + d\tau)$ when the dead time is very large ($\tau_d \gg \tau_c$), n_s is the number of photon signals, and $s(\tau)$ is the signal waveform arriving at the detector.

Equation (5) defines a case where the first photon of the echo pulse triggers the receiver, and the other photons cannot be triggered normally due to the limitation of the dead time of the receiver. In the case of a weak echo signal ($n_s \ll 1$), the dead time of the detector is no longer a restrictive factor because the detector is triggered by an event with a small number of photons in the previous signal. In formula (6), the probability function of photon detection is closely related to the waveform, so the accurate identification time of echo is the center of the waveform. For the receiving system with a very small dead time or no dead time limit, in the case of a weak echo signal, the identification error of echo time tends to 0, which is independent of echo intensity. On the other hand, for the case of a large ground slope in the laser spot, due to the large deviation of the echo pulse distribution from the waveform center, the mean square error of the identification time is relatively large, especially the error introduced by the satellite attitude. Due to the exponential term in (3), the existence of the dead time of the LiDAR receiver will lead to the asymmetric effect of the photon detection probability function. The photon trigger detector with front distribution will increase the identification error of negative time when the echo signal is a strong echo signal. When the dead time exceeds 20 ns, this effect will lead to the sharp deterioration of ranging accuracy, which cannot reach the centimeter ranging accuracy.

Using the multipixel detector array and multichannel signal processor for parallel processing, the signal photon count and noise count of each detection pixel can be significantly reduced, and the dead time effect of each channel can be reduced. Using the above two measures, the time-domain broadening effect introduced by the single-pixel detector can be significantly reduced, so as to effectively reduce the ranging system error and ranging error.

4. Simulation Analysis

4.1. Simulation of the Single-Photon LiDAR Detection Probability. The requirements of detection probability are usually related to the setting of signal contrast, receiving aperture, dead receiver time, data frame period, and distance sampling interval. When allocating system indicators, it is necessary to select the combined working conditions of signal contrast and data frame period according to specific terrain, reflectivity, and other conditions under meeting ranging accuracy. Then, select the distance sampling interval and design the load system that can meet the requirements of detection probability. Single-photon measurement based on temporal and spatial correlation coincidence is adopted. Its detection probability is mainly expanded for photon-counting events of the detection signal in the data frame. The probability of successfully identifying and acquiring the signal detection unit in a given data frame is given by

$$P_{\mathrm{acq}} = P(N_t \geq K) = 1 - e^{-N_t} \sum_{t=0}^{K-1} \frac{{N_t}^K}{K!} = 1 - e^{-CN_b} \sum_{b=0}^{K-1} \frac{(CN_b)^K}{K!}, \tag{7}$$

where N_t is the number of photon events received by the detector within a data frame and K is the data frame discrimination threshold. Similarly, the probability of erroneously identifying the noise detection unit as a signal unit is as follows:

$$P_{\mathrm{false}} = P(N_b \geq K) = 1 - e^{-N_b} \sum_{b=0}^{K-1} \frac{{N_b}^K}{K!}. \tag{8}$$

In each frame, the number of noise detection units incorrectly identified as signal detection units is given as follows:

$$N_{\mathrm{false}} = N_{\mathrm{bin}} P_{\mathrm{false}}, \tag{9}$$

where $N_{\mathrm{bin}} = \tau_g / \tau_b$ is the number of sampling intervals within the distance gate, τ_g is the echo gate width, and τ_b is the distance sampling interval. Define the statistical probability difference of the detection unit, that is, the average expected value obtained by the signal unit minus the average

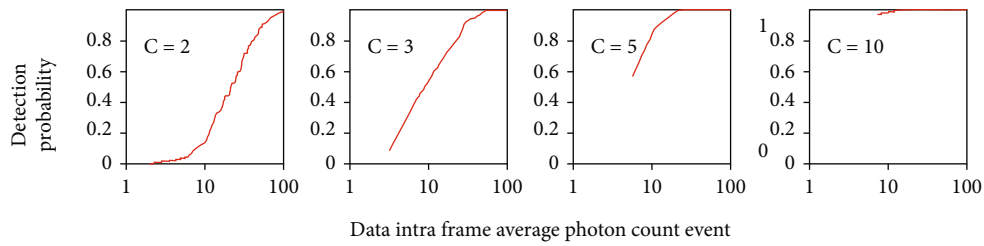

Figure 6: Relationship between detection probability and average photon-counting events inside the data frame.

Table 1: Effect analysis on signal detection for photon counting under given contrast.

Serial number	Target contrast	Data intraframe signal photon count	Detection probability	False alarm probability
1	2	80	0.999	7.664×10^{-6}
2	3	50	0.999	1.416×10^{-5}
3	5	35	0.999	8.653×10^{-6}
4	10	25	0.999	1.615×10^{-5}

expected value of the error acquisition noise unit as follows:

$$N(k) = P_{\text{acq}} - N_{\text{bin}} P_{\text{false}} = 1 - C^{\text{Kopt}} e^{-(C-1)N_b} - e^{-CN_b} \sum_{k=0}^{\text{Kopt}-1} \frac{(C^k - C^{\text{Kopt}}) N_b{}^k}{K!}, \quad (10)$$

where C^{Kopt} is optimal contrast and C^k is contrast under the data frame discrimination threshold. If the frame count threshold K is too small, too many noise detection units will be recognized as signal detection units, resulting in too small statistical probability difference of detection units ($\ll 1$) or even negative values. If the frame count threshold K is too large, the recognition algorithm will filter out too many signal photons, which will cause the statistical difference of the detection unit to be less than 1. During system design, this value needs to be selected to ensure the maximum difference in statistical probability of LiDAR detection. The relationship between the detection probability of the signal detection unit and the average photon-counting event in the data frame is shown in Figure 6 with $C = 2, 3, 5, 10$.

Different combinations of contrast and signal photon-counting events are simulated to distinguish the relationship between the detection probability in the data frame and the average photon-counting event in the data frame, as shown in Table 1. The simulation results show that the detection probability of LiDAR can reach 0.999 under several common imaging conditions in orbit. The false alarm probability reaches the lowest when the target contrast is two and the photon count value of the signal in the data frame is 80. When the target contrast is ten and the photon count value of the signal in the data frame is 25, the false alarm probability reaches the highest, which is 8.653×10^{-6}.

4.2. Simulation of the Single-Photon LiDAR Detection Illuminance. The detection illuminance of LiDAR needs to be simulated after the combination of beam homogenization and shaping system. The simulation verification method adopts the free-form surface to realize the beam homogenization, shaping, and emission. The combination of beam homogenization and shaping can realize the linear beam emission with uniform light intensity and ensure the slight divergence angle of the laser line in the transverse direction. Suppose the incident beam is a Gaussian beam and the target beam is a "linear" uniform distribution. They can be separated from variables; that is, $I_{\text{in}}(x, y)$ and $I_t(x', y')$ can be regarded as the product of two orthogonal one-dimensional illumination distributions: $I_{\text{in}}(x, y) = I_{\text{in},x}(x)$ $I_{\text{in},y}(y)$, $I_t(x', y') = I_{t,x}(x')\, I_{t,y}(y')$. If (x, y) is divided into $N \times$ grid of M: $x = x_j$, $y = y_i$, $i = 1, 2, \cdots, n$, $j = 1, 2, \cdots, m$, then one can obtain x_j' and y_i' by

$$\int_{x_1}^{x_j} I_{\text{in},x}(x)dx \int_{y_1}^{y_n} I_{\text{in},y}(y)dy = \int_{x_1'}^{x_j'} I_{t,x}\left(x'\right)dx' \int_{y_1'}^{y_n'} I_{t,y}\left(y'\right)dy', \quad (11)$$

$$\int_{x_1}^{x_m} I_{\text{in},x}(x)dx \int_{y_1}^{y_i} I_{\text{in},y}(y)dy = \int_{x_1'}^{x_m'} I_{t,x}\left(x'\right)dx' \int_{y_1'}^{y_i'} I_{t,y}\left(y'\right)dy'. \quad (12)$$

According to the above mapping relationship $x_j' = f(x_j)$ and $y_i' = f(y_i)$, one can obtain an initial vector of outgoing light as $\mathbf{O}_{i,j} = \text{Unit}(x_j' - x_j, y_i' - y_i, d)$, where the Unit symbol means to find the unit vector and d is the integral value of the data. If the incident ray vector is $\mathbf{I}_{i,J} = (0, 0_i, 1)$, then the normal vector can be calculated by

$$\left[1 + n^2 - 2n\left(\mathbf{O}_{i,j} \cdot \mathbf{I}_{i,j}\right)\right]^{1/2} \mathbf{N}_{i,j} = \mathbf{O}_{i,j} - n\mathbf{I}_{i,j}. \quad (13)$$

According to the normal vector distribution calculated by the above formula, the discrete data points of the free-form surface are obtained by the least square method. Then, the classical field tracing mode is used to simulate the detection illuminance. The waist radius of the incident beam is 2.5 mm, and twice the waist is adopted; that is, the beam energy within 10 mm in diameter is considered. The divergence half-angle of the linear distribution of the target is 0.5 degrees in the X direction and 10.3 arcseconds in the Y direction. The incident surface of the lens is a plane, and the exit surface is a free-form surface to be solved. Figure 7

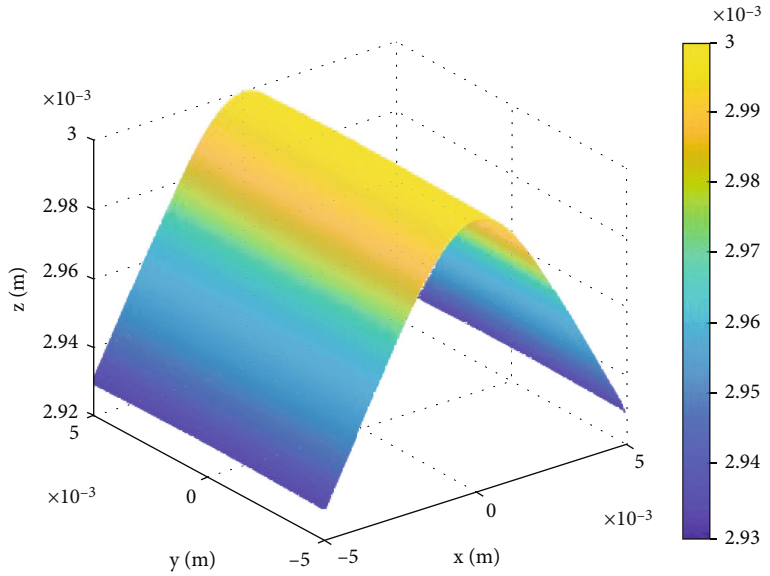

Figure 7: Optical free curved surface for laser transmitting system.

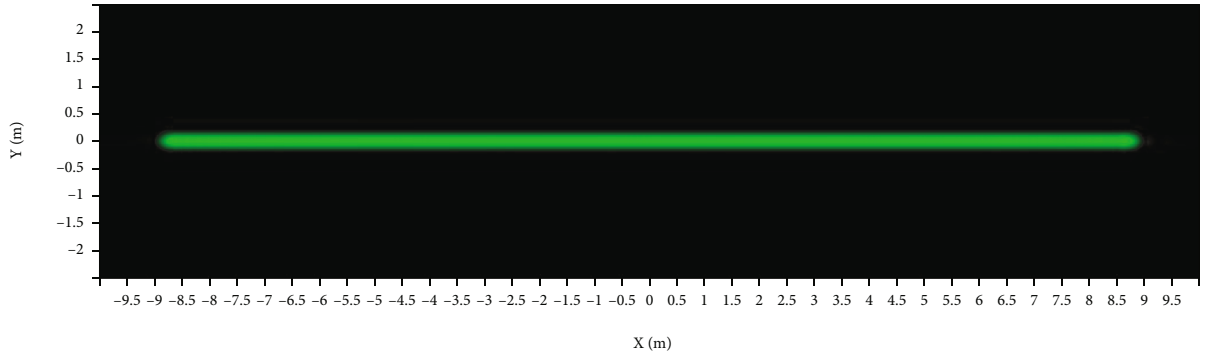

Figure 8: Illumination distribution on the position of $Z = 1$ km.

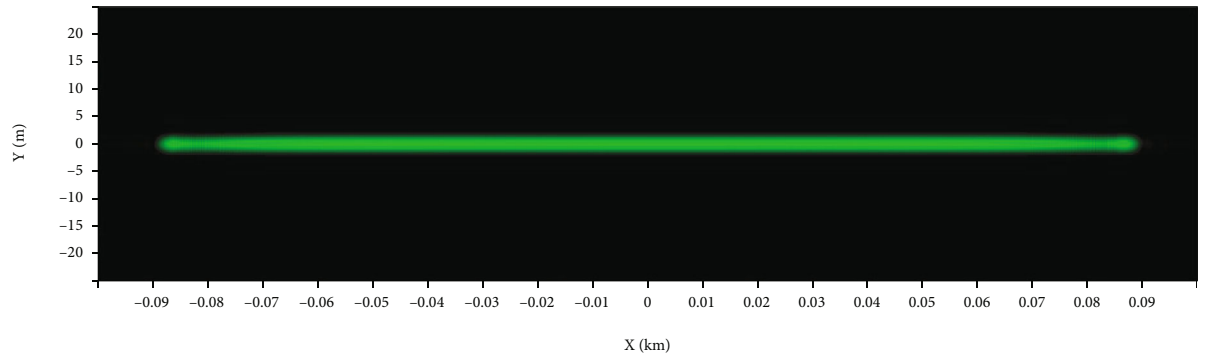

Figure 9: Illumination distribution on the position of $Z = 10$ km.

shows the calculated optical free-form surface shape, which is close to a cylindrical structure, and its vector height sag is 0.71 mm. The process of targeting from near to far is simulated. The object distance of the measured target includes 1 m, 10 m, 100 m, 1 km, 10 km, and 500 km. Figures 8–11 show the illuminance distribution at $z = 1$ km and $z = 500$ km. Through the simulation analysis, when the light source passes through the free-form surface lens, there is a process of convergence and divergence. When the object distance $z = 10$ m, the linear beam increases proportionally.

It can be seen from the statistical results of illuminance in Figure 11 that the beam intensity after free-form surface shaping starts to show an excellent linear distribution after traveling 10 m, and its distribution still has good uniformity

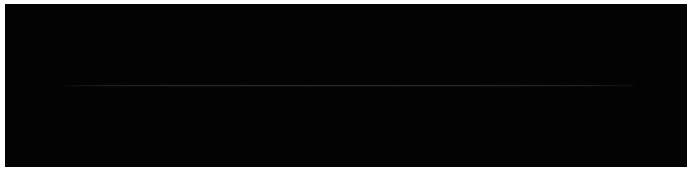

Figure 10: Illumination distribution on the position of $Z = 500$ km.

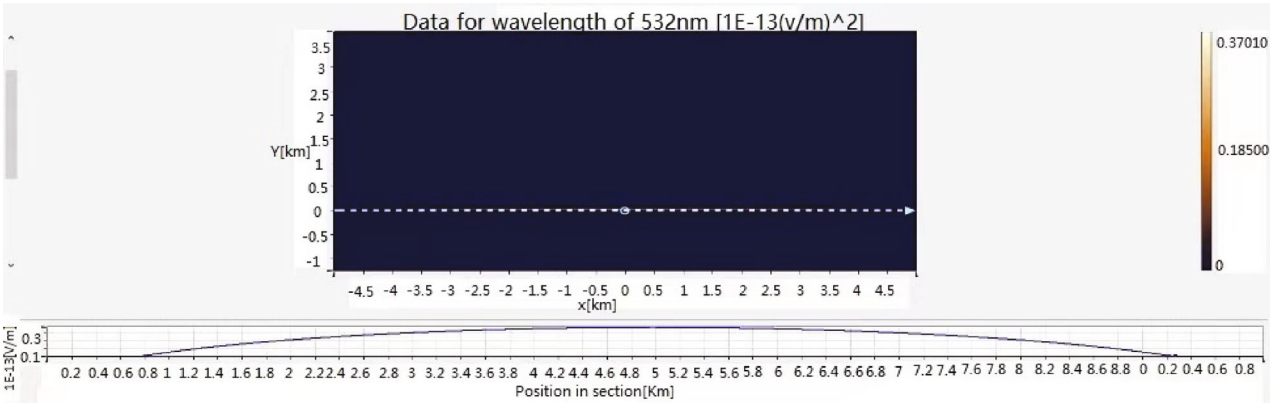

Figure 11: Laser illumination statistics on the position of $Z = 500$ km.

when the object distance reaches 500 km. This distribution is conducive to the full utilization of laser energy at the detection end, and loss reduces the laser's energy after ultra-long-distance propagation as much as possible.

The simulation shows that the dead time of the detector is linearly inversely proportional to the receiving aperture [22, 23]. Under the premise of ensuring the same signal contrast, the allowable receiving area can be increased by about 4~6 times compared with the single-pixel detector using the multielement detector. For different contrast and signal photon-counting events, the more detection counts, the greater the detection probability, and the higher the contrast, the earlier the detection probability reach the peak under the same signal photon-counting event [24, 25]. When the contrast is five and the signal photon count in the data frame is 35, the photon detection probability reaches the maximum, and the false alarm rate is the lowest. Therefore, to achieve high detection probability and minimum false alarm rate, the comprehensive influence of photon counting, dead time, and contrast needs to be considered in the design process. At the system level, according to the influence of detector dead time on ranging accuracy index, the detection probability and detection illuminance of single-photon LiDAR are simulated and analyzed, and the detection illuminance distribution of LiDAR under different object distances is obtained.

5. Conclusion

In this paper, the influence of the slow time of a single-photon detector on ranging accuracy, detection probability, and detection illumination in tandem single-photon LiDAR ranging is modeled and simulated. The influence relationship of detector dead time is established under different detection contrast. The simulation shows that by reasonably controlling the dead time and effective receiving aperture of the detector and using the free-form surface optical receiving system, the shaped beam intensity shows an excellent linear distribution after propagating a distance of 10 m. Its distribution still has good uniformity outside the object distance of 500 km, which proves the effectiveness and rationality of the simulation model of this method.

Data Availability

The data used to support the findings of this study are included within the article.

Conflicts of Interest

We declare that we have no conflict of interest.

References

[1] D. Renker and E. Lorenz, "Advances in solid state photon detectors," *Journal of Instrumentation*, vol. 4, no. 4, p. P04004, 2009.

[2] G. Q. Zhang, X. B. Hu, C. Z. Hu et al., "Demonstration of a silicon photomultiplier with bulk integrated quenching resistors on epitaxial silicon," *Nuclear Instruments and Methods in Physics Research Section A: Accelerators, Spectrometers, Detectors and Associated Equipment*, vol. 621, no. 1-3, pp. 116–120, 2010.

[3] K. Shi, C. Liu, Z. Sun, and X. Yue, "Coupled orbit-attitude dynamics and trajectory tracking control for spacecraft electromagnetic docking," *Applied Mathematical Modelling*, vol. 101, pp. 553–572, 2022.

[4] C. Liu, X. Yue, J. Zhang, and K. Shi, "Active disturbance rejection control for delayed electromagnetic docking of spacecraft

in elliptical orbits," *IEEE Transactions on Aerospace and Electronic Systems*, vol. 58, no. 3, pp. 2257–2268, 2022.

[5] K. Shi, C. Liu, J. D. Biggs, Z. Sun, and X. Yue, "Observer-based control for spacecraft electromagnetic docking," *Aerospace Science and Technology*, vol. 99, article 105759, 2020.

[6] C. Liu, G. Vukovich, Z. Sun, and K. Shi, "Observer-based fault-tolerant attitude control for spacecraft with input delay," *Journal of Guidance, Control, and Dynamics*, vol. 41, no. 9, pp. 2041–2053, 2018.

[7] X. Shao, Q. Hu, Z. H. Zhu, and Y. Zhang, "Fault-tolerant reduced-attitude control for spacecraft constrained boresight reorientation," *Journal of Guidance, Control, and Dynamics*, pp. 1–15, 2022.

[8] X. Shao and Q. Hu, "Immersion and invariance adaptive pose control for spacecraft proximity operations under kinematic and dynamic constraints," *IEEE Transactions on Aerospace and Electronic Systems*, vol. 57, no. 4, pp. 2183–2200, 2021.

[9] C. Liu, X. Yue, and Z. Yang, "Are nonfragile controllers always better than fragile controllers in attitude control performance of post-capture flexible spacecraft?," *Aerospace Science and Technology*, vol. 118, article 107053, 2021.

[10] J. M. Stoker, Q. A. Abdullah, A. Nayegandhi, and J. Winehouse, "Evaluation of single photon and Geiger mode LiDAR for the 3D elevation program," *Remote Sensing*, vol. 8, no. 9, p. 767, 2016.

[11] A. Swatantran, H. Tang, T. Barrett, P. DeCola, and R. Dubayah, "Rapid, high-resolution forest structure and terrain mapping over large areas using single photon lidar," *Scientific Reports*, vol. 6, no. 1, pp. 1–12, 2016.

[12] K. Y. Shrestha, W. E. Carter, K. C. Slatton, and T. K. Cossio, "Shallow bathymetric mapping via multistop single photoelectron sensitivity laser ranging," *IEEE Transactions on Geoscience and Remote Sensing*, vol. 50, no. 11, pp. 4771–4790, 2012.

[13] N. A. Forfinski-Sarkozi and C. E. Parrish, "Analysis of MABEL bathymetry in Keweenaw Bay and implications for ICESat-2 ATLAS," *Remote Sensing*, vol. 8, no. 9, p. 772, 2016.

[14] B. Du, C. Pang, D. Wu et al., "High-speed photon-counting laser ranging for broad range of distances," *Scientific Reports*, vol. 8, no. 1, p. 4198, 2018.

[15] T. Cossio, K. C. Slatton, W. Carter, K. Shrestha, and D. Harding, "Predicting topographic and bathymetric measurement performance for low-SNR airborne lidar," *IEEE Transactions on Geoscience and Remote Sensing*, vol. 47, no. 7, pp. 2298–2315, 2009.

[16] L. Xue, D. Zhai, Y. Li et al., "Ranging capability analysis for laser ranging system using superconducting nanowire detectors," *Acta Optica Sinica*, vol. 36, no. 3, p. 0304001, 2016.

[17] Q. Li, J. Degnan, T. Barrett, and J. Shan, "First evaluation on single photon-sensitive lidar data," *Photogrammetric Engineering and Remote Sensing*, vol. 82, no. 7, pp. 455–463, 2016.

[18] C. Yao, W. Chen, and G. Zang, "Accurate measurement of sea surface in an airborne laser bathymetry," *Infrared and Laser Engineering*, vol. 32, no. 4, pp. 351–355, 2003.

[19] A. Axelsson, "Rapid topographic and bathymetric reconnaissance using airborne LiDAR," in *Proceedings Volume 7835, Electro-Optical Remote Sensing, Photonic Technologies, and Applications IV*, pp. 39–48, Toulouse, France, 2010.

[20] C. Liu, X. Yue, K. Shi, and Z. Sun, "Inertia-free attitude stabilization for flexible spacecraft with active vibration suppression," *International Journal of Robust and Nonlinear Control*, vol. 29, no. 18, pp. 6311–6336, 2019.

[21] C. Liu, K. Shi, X. Yue, and Z. Sun, "Inertia-free saturated output feedback attitude stabilization for uncertain spacecraft," *International Journal of Robust and Nonlinear Control*, vol. 30, no. 13, pp. 5101–5121, 2020.

[22] M. Ghioni, A. Gulinatti, I. Rech, F. Zappa, and S. Cova, "Progress in silicon single-photon avalanche diodes," *IEEE Journal of Selected Topics in Quantum Electronics*, vol. 13, no. 4, pp. 852–862, 2007.

[23] L. Zheng-Ping, X. Huang, Y. Cao et al., "Single-photon computational 3D imaging at 45 km," *Photonics Research*, vol. 8, no. 9, pp. 1532–1540, 2020.

[24] T. Yin, N. Lauret, and J. P. Gastellu-Etchegorry, "Simulation of satellite, airborne and terrestrial LIDAR with DART (II): ALS and TLS multi-pulse acquisitions, photon counting, and solar noise," *Remote Sensing of Environment*, vol. 184, pp. 454–468, 2016.

[25] J. J. Degnan, "Scanning, multibeam, single photon Lidars for rapid, large scale, high resolution, topographic and bathymetric mapping," *Remote Sensing*, vol. 8, no. 11, p. 958, 2016.